Nanoscale Res Lett (2010) 5:1952–1961
DOI 10.1007/s11671-010-9732-9

NANO EXPRESS

Highly Efficient Near-IR Photoluminescence of Er^{3+} Immobilized in Mesoporous SBA-15

Y. L. Xue · P. Wu · Y. Liu · X. Zhang · L. Lin · Q. Jiang

Received: 23 February 2010 / Accepted: 4 August 2010 / Published online: 24 August 2010

Abstract SiO_2 mesoporous molecular sieve SBA-15 with the incorporation of erbium ions is studied as a novel type of nanoscopic composite photoluminescent material in this paper. To enhance the photoluminescence efficiency, two schemes have been used for the incorporation of Er^{3+} where (1) Er^{3+} is ligated with bis-(perfluoromethylsulfonyl)-aminate (PMS) forming $Er(PMS)_x$-SBA-15 and (2) Yb^{3+} is codoped with Er^{3+} forming Yb-Er-SBA-15. As high as $11.17 \times 10^{-21} cm^2$ of fluorescent cross section at 1534 nm and 88 nm of "effective bandwidth" have been gained. It is a 29.3% boost in fluorescent cross section compared to what has been obtained in conventional silica. The upconversion coefficient in Yb-Er-SBA-15 is relatively small compared to that in other ordinary glass hosts. The increased fluorescent cross section and lowered upconversion coefficient could benefit for the high-gain optical amplifier. Finally, the Judd–Ofelt theory has also been used for the analyses of the optical spectra of $Er(PMS)_x$-SBA-15.

Keywords Mesoporous molecular sieve SBA-15 · Rare-earth ions · Photoluminescence · Cooperative upconversion · Judd–Ofelt theory

Y. L. Xue (✉) · L. Lin · Q. Jiang
Department of Electronic Engineering, East China Normal University, 500 Dongchuan Road, Shanghai 200241, China
e-mail: ylxue@ee.ecnu.edu.cn

P. Wu · Y. Liu · X. Zhang
Shanghai Key Laboratory of Green Chemistry and Chemical Processes, East China Normal University, 500 Dongchuan Road, Shanghai 200241, China

Introduction

Lanthanide ion Er^{3+} has usually been immobilized in disordered host materials like silicas and aluminosilicates for applications in optical communications. In recent years, micelle-templated silicas and aluminosilicates have attracted great attentions as hosts with ordered mesopores and micropores for their potential for better optical properties [1, 2]. Among them, mesoporous silica has been regarded as an ideal candidate due to its appealing textural properties, appreciable thermal and hydrothermal stability, tunable pore size, and alignment, while microporous aluminosilicate zeolite exhibits good features of highly crystalline framework, ordered sub-nanopores with pore diameter ranging from 1 to 20 Å, and high hydrophobicity. In particular, mesoporous silica SBA-15 synthesized using Zhao's method has highly ordered hexagonal mesopores with parallel channels and adjustable pore size in the range of 5–30 nm [3]. Lanthanide ions have been reported to be immobilized in the mesoporous silica like MCM-41, MCM-48, and SBA-15 [4–6] or microporous aluminosilicates like faujasite-type zeolites [7, 8].

In general, the 4f–4f transitions are electric dipole forbidden for the free lanthanide ions. After the incorporation of lanthanide ions into host lattices, the electric-dipole transitions induced by odd-parity terms in the local field become weakly allowed, although their strength is still weak. Hence, usually efficient photoluminescence of lanthanide ions cannot be obtained from their direct incorporation into mesoporous silicas or microporous aluminosilicates. To date, two approaches have been used to enhance the photoluminescent efficiency. One is based on the work of Wada and the coworkers [7], in which a low vibrational environment by excluding the high vibrational bonds such as

C–H and O–H from the surroundings of lanthanide ions has been adopted. Lanthanide ion Nd^{3+} is ligated with bis-(perfluoromethylsulfonyl)aminate (PMS) to form a low vibrational ligand $Nd(PMS)_x$. This approach has been proved to be effective to the Nd^{3+} complex captured in zeolite nanostructure [8], but not yet to other lanthanide ions.

The other makes use of the antenna effect (or sensitization process) [9]. Lanthanide ions are incorporated into organic chromophores to form the lanthanide complexes that are covalently linked to the inner walls of the mesoporous silica's pores. The absorption coefficients of organic chromophores are considered to be orders of magnitude higher than that of lanthanide ions. And organic chromophores are able to control and even enhance the photophysical properties of lanthanide ions. However, the usage of organic chromophores is often constrained to mesoporous materials because their molecules are usually too large to the pores of microporous materials. So far, appropriate organic chromophores all incorporated in mesoporous silicas have been found to some lanthanide ions, such as Nd^{3+}, Yb^{3+}, and Eu^{3+} [4–6], but not yet to Er^{3+} since its emission in mesoporous silicas is still weak and does not exhibit the saddle-shaped characteristic spectra [5, 6].

Similarly to the sensitization of organic chromophores to lanthanide ions, another lanthanide ion Yb^{3+} can be codoped with the luminescent center Er^{3+} to sensitize Er^{3+} since state $^2F_{5/2}$ of Yb^{3+} is in the similar energy level with state $^4I_{11/2}$ of Er^{3+} and the absorption of $^2F_{5/2}$ around 980 nm is much stronger and broader than that of $^4I_{11/2}$ [10]. It is also noted that codoping of Yb^{3+} is an effective way to enhance the photoluminescence in microporous aluminosilicates since the large molecules of organic chromophores cannot enter into the small pores of microporous aluminosilicates. Such sensitization of Yb^{3+} to Er^{3+} has been widely used in disordered silicas and aluminosilicates, but not yet in mesoporous silica and microporous aluminosilicates.

In addition, since the nonhomogeneous distribution of immobilized Er^{3+} is the reason causing clustering which results in cross relaxations and degrades the photoluminescence, codoping Yb^{3+} to form low vibrational $Er(PMS)_x$ complexes and the walls of mesopores and cages in SBA-15 can play the roles of dispersing Er^{3+}, providing a more homogeneous distribution for Er^{3+} ions and therefore suppressing the cross relaxation processes.

In this paper, a study was performed on mesoporous SBA-15 with Er^{3+} incorporation. Two approaches have been adopted to enhance the photoluminescence of Er^{3+} ions in which (1) Er^{3+} is ligated with PMS forming $Er(PMS)_x$-SBA-15 and (2) Yb^{3+} is codoped forming Yb-Er-SBA-15. The highly efficient near-IR emission of Er^{3+} has been observed.

Experimental Section

Synthesis of Mesoporous SBA-15

SBA-15 was hydrothermally synthesized in an acidic medium using triblock copolymer P123 as template and tetraethyl orthosilicate (TEOS) as silica source. P123 (24 g) was first dissolved in deionized water (630 mL). TEOS (51 g) and 37wt% HCl (140 mL) were then added into above aqueous solution to form a synthetic gel after 24-h stirring. The gel was then heated in a Teflon-lined autoclave under static conditions at 100°C for 20 h. The product was gathered by filtration and washed with deionized water. SBA-15 was then obtained after drying at 100°C and calcinating in air at 550°C for 5 h to burn off the template [3].

Synthesis of $Er(PMS)_x$-SBA-15 Complex

Using SBA-15 as a nanoreactor, we have impregnated Er^{3+} ions into the mesopores of SBA-15 first, and then further functionalized these Er^{3+} species with PMS to form $Er(PMS)_x$ complex. 0.1 g of SBA-15 sample was stirred in 30 mL of 0.0025, 0.005, or 0.0075 mol/L $Er(Ac)_3$ $4H_2O$ solution to form a homogenous mixture. It dried up after heating in an oven overnight to obtain Er^{3+} impregnated sample, Er-SBA-15. The Er species were probably immobilized on the silica walls through an interaction with the silanols that were abundant in mesoporous silica. The sample was then outgassed in a cell at 150°C for 30 min. After cooling to 100°C, the sample was exposed to a PMS vapor for 30 min and further evacuated at 150°C for 30 min to remove any PMS physically adsorbed. The $Er(PMS)_x$ were then presumed to form inside the mesopores of SBA-15 to take a possible chemical structure as shown in Fig. 1. The $Er(PMS)_x$-SBA-15 sample thus prepared was stored under vacuum to avoid moisture.

Synthesis of Yb-Er-SBA-15

SBA-15 was stirred with 30 mL of 0.0312 g, i.e. 0.0075 mol/L, $Er(Ac)_3{\cdot}4H_2O$ solution, into which 0.0673 g, 0.1121 g, 0.1794 g, or 0.2425 g of $Yb_2(CO_3)_3{\cdot}4H_2O$ was

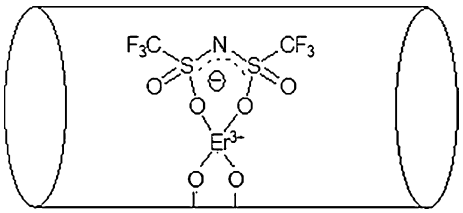

Fig. 1 Model of $Er(PMS)_x$ inside a mesopores of SBA-15

added to carry out co-impregnation of Er and Yb species. The molar ratio of Er^{3+} to Yb^{3+} was 1:3,1:5,1:8, and 1:10, respectively. After drying at 60°C overnight, the sample impregnated with both Er^{3+} and Yb^{3+} was obtained, Yb-Er-SBA-15. Meanwhile, the $(SiO)_xEr$ or $(SiO)_xYb$ species were also formed inside the mesopores due to the existence of large amount of SiOH on the surface of inner pores.

Characterization Methods

The inductively coupled plasma (ICP) measurement was carried out for the Er^{3+} and Yb^{3+} contents on Thermo IRIS Intrepid II XSP atomic emission spectrometer. Small-angle X-ray diffraction patterns were recorded with a Germany Bruker D8 Advance diffractometer using Cu Kα radiation (40 kV, 200 mA) at a step width of 0.01°. Nitrogen (N_2) adsorption–desorption isotherms were measured at 77 K on a Quantachrome Autosorb-3B instrument after the samples were outgassed at 473 K in vacuum at least for 10 h prior to investigation. SEM and TEM images were measured on a Hitachi S-4800 scanning electron microscope and a JEOL JEM-2010 transmission electron microscope, respectively. EDS spectra were obtained on an EMAX. The absorption spectra were measured on Perkin–Elmer Lambda 900 UV/VIS/NIR spectrometer. The emission spectra were recorded on Jobin-Yvon Fluolog-3 fluorescence spectrometer equipped with a 980 nm picosecond laser diode (LD) from HaiDer Company as excitation source. Refractive index measurement was done on a SC620 elliptical polarization spectrometer.

Experimental Results and Discussion

$Er(PMS)_x$ Complexes Functionalized SBA-15 Hybrid Materials $Er(PMS)_x$-SBA-15

Er^{3+} Concentration

The Er^{3+} contents in SBA-15 were obtained from ICP measurement as 3.17, 6.34, and 9.51wt%, which correspond to the concentration of 9.03×10^{19}, 1.81×10^{20}, and 2.71×10^{20}ions/cm3, respectively. Due to the high porosity and larger specific surface area (>700 m^2/g) in SBA-15 system the obtained Er^{3+} contents in weight percent are relatively larger than that in conventional silica (ca. 300 m^2/g).

Powder XRD, TEM, N2 Adsorption, and EDS

Figure 2 shows the powder XRD patterns for SBA-15 starting material, Er-SBA-15 and $Er(PMS)_x$-SBA-15. The unmodified SBA-15 sample exhibits three diffraction in the

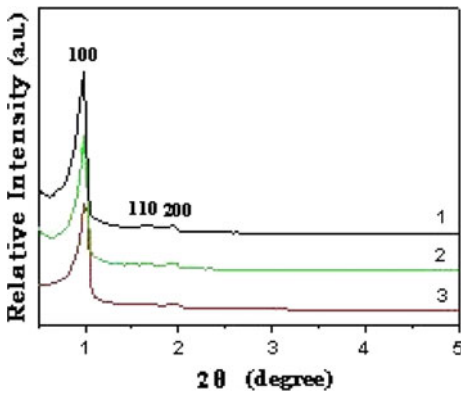

Fig. 2 Powder XRD patterns of (*1*) SBA-15, (*2*) Er-SBA-15, and (*3*) $Er(PMS)_X$-SBA-15

2θ range 2–3°, indexed for a hexagonal cell as (100), (110), (200). Upon inclusion of Er^{3+} ions, the characteristic diffractions are still observed at about the same positions with similar intensities, demonstrating that the long-term hexagonal symmetry of the mesopores is preserved. After the subsequent functionalization of Er-SBA-15 complex with PMS, inapparent shift toward a larger angle indicates shrinkage of the unit cell parameter due to a slight dehydroxylation, but the hexagonal symmetry of the mesopores is still preserved. The attenuation of the X-ray peaks, especially after the functionalization forming the bulky Er^{3+} complex, is not interpreted as a loss of long-range order but rather to a reduction in the X-ray scattering contrast between the silica walls and pore-filling materials.

The TEM micrographs in Fig. 3 provide further proof for the preservation of hexagonal mesostructure in $Er(PMS)_x$-SBA-15. As shown in the figure, for the $Er(PMS)_x$ complexes functionalized SBA-15 regular hexagonal arrays of long-term uniform channels still exist with 8 nm mesopore diameter. Although the incorporation of Er species was carried out in an aqueous solution, the mesostructure and the pore array are almost intact. Thus, we have obtained very stable materials after various post-modifications. It should be pointed out that no clustering of Er^{3+} complexes or Er^{3+} ions and no blocking to the mesopores can be seen in Fig. 3.

Figure 4 displays the N_2 adsorption–desorption isotherms and pore diameter distributions of SBA-15 before and after the inclusion of Er^{3+} ions. Both of them show typical reversible type IV isotherms with H1-type hysteresis loop, characteristic of ordered mesoporous materials according to the IUPAC classification [11]. Measurement of the isotherms revealed a lower nitrogen uptake for Er-SBA-15 compared with SBA-15, with the specific surface area calculated with the BET method reduced from 704 to 464 m^2/g, pore volume reduced from 0.96 to 0.52 cm^3/g, and pore diameter calculated with the BJH method reduced from 8.3 to 7.5 nm. The reduction in these parameters

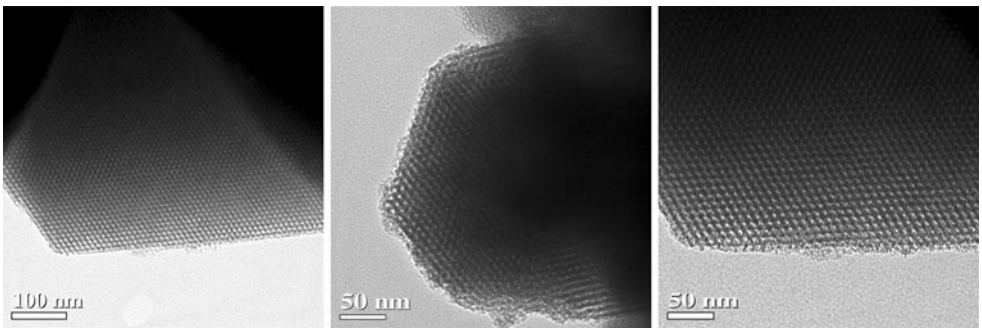

Fig. 3 TEM images of (*1*) SBA-15, (*2*) Er-SBA-15, and (*3*) Er(PMS)$_X$-SBA-15

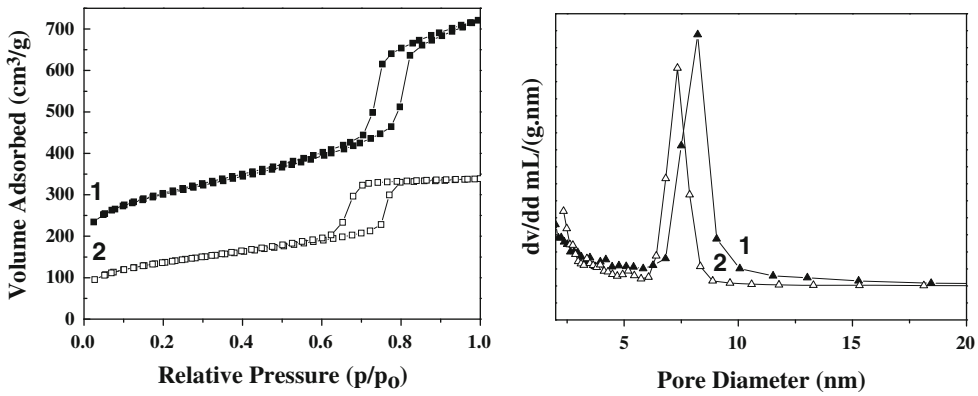

Fig. 4 N_2 adsorption–desorption isotherms and pore size distributions (*1*) SBA-15; (*2*) Er-SBA-15

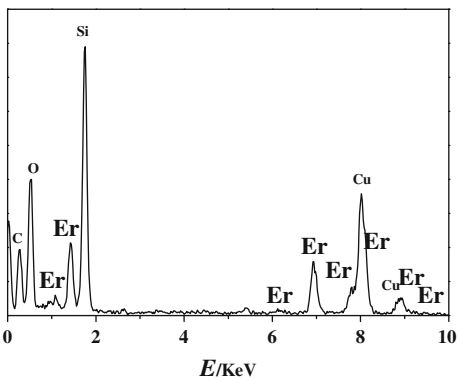

Fig. 5 EDS energy spectrum of Er(PMS)$_x$-SBA-1

arises from the inclusion, dispersion, and anchoring of Er^{3+} ions in the SBA-15 pores. As shown in Fig. 1, the Er species are incorporated in the mesopores probably through the chemical bonding with the silanols. These species occupy the spaces of the pores and make they partially blocked. This then reasonably leads to much smaller values of the surface area, pore volume and pore size for Er-SBA-15 in comparison with the parent SBA-15.

The EDS energy spectrum of Er(PMS)$_x$-SBA-15 in Fig. 5 clearly displays the energy distribution of Er^{3+}. That almost same diagrams obtained from the measurement at different parts of the sample demonstrates a uniform inclusion of Er^{3+} complexes in the pores of SBA-15.

Index of Refraction

The dispersion measurement in Fig. 6 shows a very small range of variation for refractive index from 1.096 to 1.103 for the wavelength ranging from 800 to 1700 nm. In comparison with conventional silica, the mesoporous silica of SBA-15, containing a large quantity of well-ordered mesopores, is considered to have a higher porosity. This would result in a relatively smaller index of refraction.

Absorption and Photoluminescence

Figure 7 displays two similar absorption spectra from (1) original SBA-15 with the direct inclusion of Er^{3+} ions and (2) Er(PMS)$_x$ complexes functionalized SBA-15. It demonstrates no obvious affection from PMS to the absorption spectrum of Er^{3+} ions. Compared to the absorption spectra of Er^{3+} in conventional disordered silica, no more difference was found in that of Er(PMS)$_x$-SBA-15, except the double absorption peaks at 1502.2 and 1531.0 nm. This illustrates the electrons in the excited state $^4I_{13/2}$ tend to centralize in two Stark sub-states.

Figure 8 shows the emission spectra of $^4I_{13/2} \rightarrow {}^4I_{15/2}$ transition of Er^{3+} ions for (1) Er-SBA-15 with Er^{3+} concentration 1.81×10^{20}ions/cm^3(curve 1) and (2) Er(PMS)$_x$-SBA-15 with three Er^{3+} concentrations 9.03×10^{19},

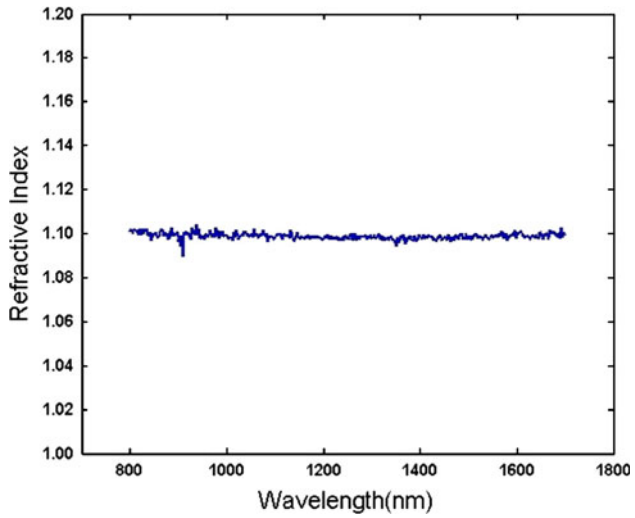

Fig. 6 Refractive index of $Er(PMS)_x$-SBA-15

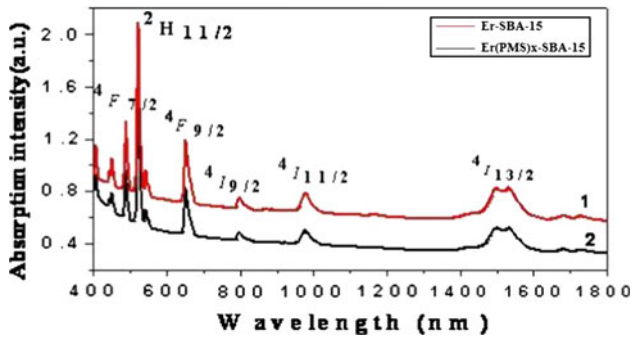

Fig. 7 Absorption spectra of (*1*) Er-SBA-15 and (*2*) $Er(PMS)_x$-SBA-15

1.81×10^{20}, and 2.71×10^{20}ions/cm^3 (curves 2, 3, and 4), respectively. In contrast to the poor emission from Er-SBA-15, all $Er(PMS)_x$-SBA-15 samples show remarkably stronger emission. This result has led to a conclusion that PMS in the SBA-15 mesopores can enhance the emission. PMS is playing two important roles that (1) the low vibrational ligands $Er(PMS)_x$ can effectively retard the coordination of Er^{3+} with OH^- groups existing on the inner walls of the pores which is with high vibrational energy and causes the de-excitation of excited Er^{3+} ions, and (2) the ligands $Er(PMS)_x$ also retard the aggregation of Er^{3+} ions. The negative effects of coordinating lanthanide ions with H_2O molecules and hydroxyl groups in zeolites on its emission were already reported [12, 13].

At the Er^{3+} concentration 1.81×10^{20}ions/cm^3(curve 3 in Fig. 8), the emission intensity reaches maximum with peak cross section $\sigma_{em} = 10.9 \times 10^{-21}$cm^2 in Fig. 9. Compared with the peak emission cross section 7.9×10^{-21}cm^2 of Er^{3+} in conventional silica, our result has a 27.5% increase [14]. With a further increase in the Er^{3+} concentration to 2.71×10^{20}ions/cm^3 (curve 4 in Fig. 8),

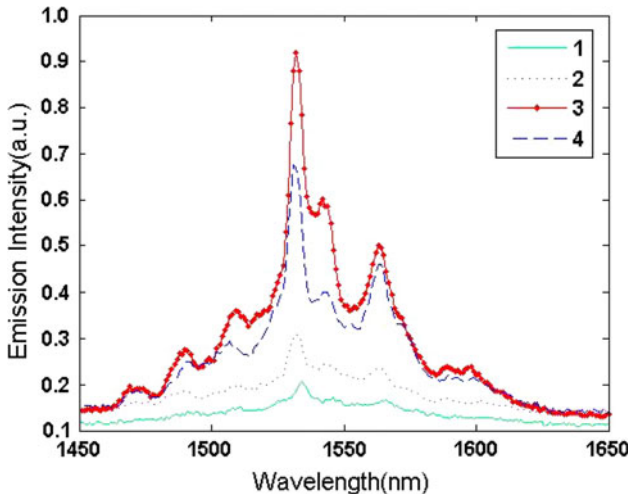

Fig. 8 Fluorescence spectra of (*1*) Er-SBA-15 with Er^{3+} concentrations of 1.81×10^{20}ions/cm^3 (*curve* 1) and (*2*) $Er(PMS)_x$-SBA-15 with Er^{3+} concentrations of 9.03×10^{19}, 1.81×10^{20}, and 2.71×10^{20}ions/cm^3, respectively (*curves* 2, 3 and 4)

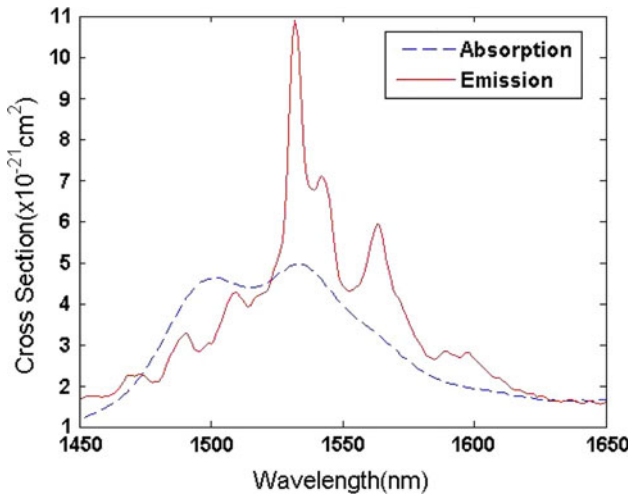

Fig. 9 Absorption and emission cross sections of $Er(PMS)_x$-SBA-15

instead the emission intensity decreases due to the Er^{3+} aggregation-induced quenching.

In addition, except a primary emission peak at 1531.8 nm as usual, an obvious subsidiary peak splits out at 1563.0 nm and three small subsidiary peaks turn up at 1509.4, 1491.0, and 1468.5 nm, respectively. This is an obvious difference to the emission of Er^{3+} in bulk glass materials [14] where all subsidiary peaks are smoothly linked to the primary peak and almost cannot be distinguished individually. In general, when the particle size of a material is reduced to the nano range, the quantum size effects may arise with the presence of splitting of spectra and shifting of spectrum peaks [15]. The splitting of the subsidiary emission peaks in Figs. 8 and 9 demonstrates the existence of quantum size effects in $Er(PMS)_x$-SBA-15. It can also be discerned that at Er^{3+}

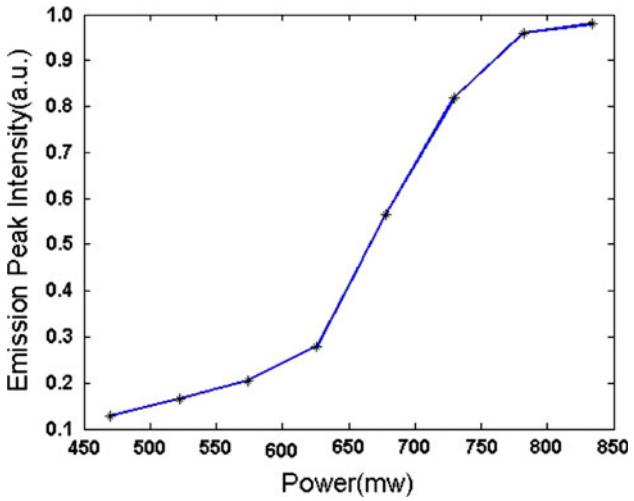

Fig. 10 Variation of peak emission intensity with pump power

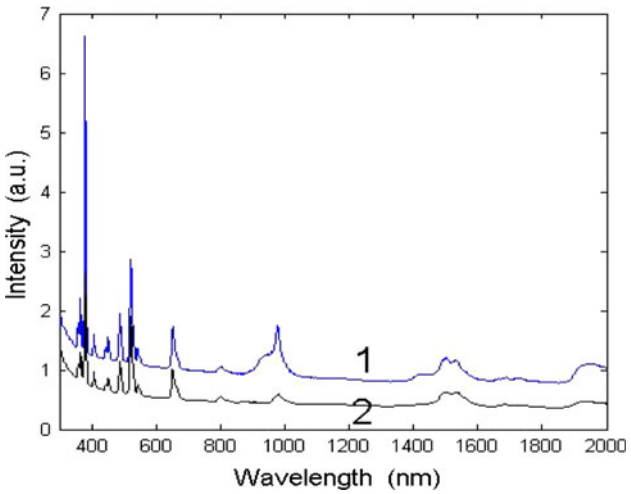

Fig. 11 Absorption spectra of (*1*) Yb-Er-SBA-15 and (*2*) Er-SBA-15

concentration 1.81×10^{20}ions/cm^3 and 2.71×10^{20}ions/cm^3, the FWHM bandwidths are 20 and 53 nm, respectively. The split of the subsidiary peak is the reason corresponding to these narrower FWHM bandwidths.

Figure 10 displays the variation of emission peak intensity of Er(PMS)$_x$-SBA-15 with the 980 nm pump strength at the Er^{3+} concentration 9.03×10^{19} ions/cm^3. The tendency of the variation is that the emission peak intensity increases almost linearly while the pump strength increases from 469 to 834 mW. In addition, under such a strong 980 nm excitation, there is no any visible light seeable by naked eyes in the dark environment. Upconversion is very weak.

Yb^{3+} and Er^{3+} Co-doped Mesoporous SBA-15 Hybrid Materials Yb-Er-SBA-15

Absorption and Photoluminescence

Figure 11 shows a comparison of the absorption spectra for (1) original SBA-15 with the inclusion of both Yb^{3+} and Er^{3+} ions and (2) original SBA-15 with the only inclusion of Er^{3+} ions. No more difference can be found between these two spectra except the stronger and broader absorption around 980 nm for Yb-Er-SBA-15.

Figure 12 shows emission spectra of Yb-Er-SBA-15 under the 980 nm pump excitation where Yb^{3+} and Er^{3+} concentration ratio is 1:10 (blue curve), 1:8 (green curve), 1:5 (red curve) and 1:3 (yellow curve), respectively. It can be seen clearly that following the increment of Yb^{3+} proportion, the emission intensity incessantly increases, indicating that the denser the Yb^{3+} ions, the more the excited electrons of Yb^{3+} ions are transferred to Er^{3+} and the stronger the population inversion between excited state $^4I_{13/2}$ and ground state $^4I_{15/2}$ of Er^{3+} ions is. But the

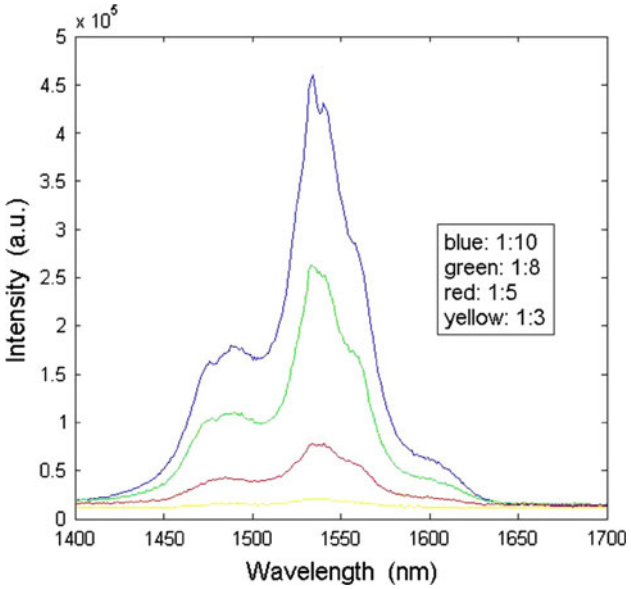

Fig. 12 Fluorescence spectra of Yb-Er-SBA-15 under the 980 nm pump excitation for Er^{3+}/Yb^{3+} concentration ratios of 1:10 (*blue*), 1:8 (*green*), 1:5 (*red*), and 1:3 (*yellow*)

increment is not endless. Our experiments were repeated many times for high Yb^{3+} ratio specimen (Er^{3+}:Yb^{3+} = 1:12 and 1:14) and the results showed the strongest emission occurred at the ratio of Er^{3+}:Yb^{3+} = 1:10. As Yb^{3+} ions have a much lower melting temperature (819°C) than Er^{3+} ions (1522°C), the high Yb^{3+} ratio specimens are also with a reduced melting temperature and easy to be burned under the pump excitation. Figure 13 shows the absorption and emission cross sections for the specimen with Er^{3+}:Yb^{3+} = 1:10 in which the emission cross section reaches maximum with peak value of $\sigma_{em} = 11.17 \times 10^{-21}$cm^2. This is 29.3% higher than the results in ordinary silica [14] and 2.42% higher than that in Er(PMS)$_x$-SBA-15, respectively.

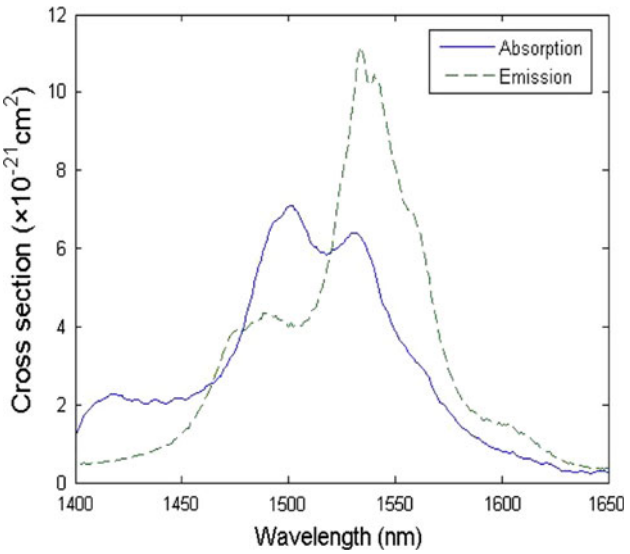

Fig. 13 Absorption and emission cross sections of Yb-Er-SBA-15 for 1:10 Er^{3+}/Yb^{3+} concentration ratio

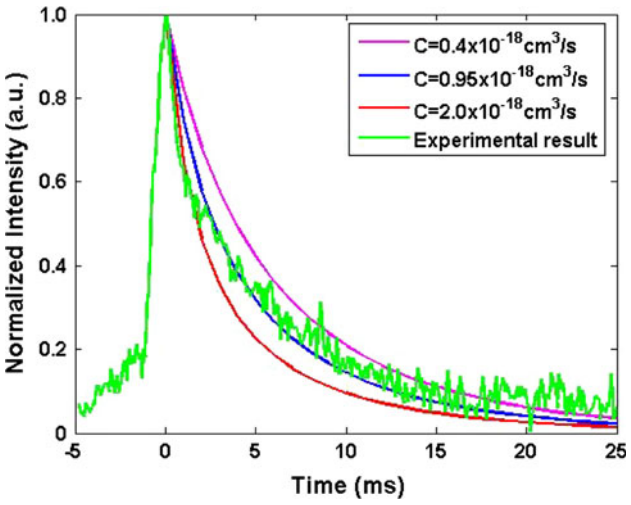

Fig. 14 Experimental fluorescence decay curve and theoretical simulation

In Fig. 12, although the too high emission peak corresponds to a not too wide FWHM bandwidth 45 nm (1519–1564 nm) at 5.59×10^{-21}cm^2, if the left subsidiary peak is taken into account, the "effective bandwidth" could be 88 nm (1483–1570 nm) in total at cross section 4.03×10^{-21}cm^2. This cross section is close to half of the maximum emission cross section 3.95×10^{-21}cm^2 in conventional silica where the FWHM is 35 nm usually. This means when one obtains an amplifier gain (proportional to the emission cross section) which equals to the gain of a commercial erbium-doped fiber amplifier (EDFA) made from conventional silica, one can obtain a much broader bandwidth 88 nm in Yb-Er-SBA-15. Therefore, Yb-Er-SBA-15 is promise to the applications of both high output lasers and broadband amplifiers.

Fluorescence Lifetime

The green curve in Fig. 14 shows the deexcitation process of the excited state of Er^{3+} ions in Yb-Er-SBA-15 after the withdraw of the pump. The fluorescence lifetime can be obtained from the decay curve as 9.0 ms. The noise shown in the experiment curve comes from the powder specimen. Usually powder samples cause more noise than bulk samples.

Theoretical Treatment

Simulation to Upconversion Coefficient

Cooperative upconversion is an energy-transfer process between two excited Er^{3+} ions in close proximity that interact in the $^4I_{13/2}$ manifold [16]. One excited Er^{3+} ion (donor) transfers energy to the other excited ion (acceptor), causing the acceptor to be promoted to the $^4I_{9/2}$ manifold and the donor to be deexcited to ground state $^4I_{15/2}$ nonradiatively. The excited Er^{3+} ions in the $^4I_{9/2}$ manifold will nonradiatively decay to the $^4I_{15/2}$ manifold. This reduces the Er^{3+} population in the $^4I_{13/2}$ manifold. In the high Er^{3+} concentration case, the cooperative upconversion process may be serious in reducing the population of metastable state $^4I_{13/2}$ and causing the reduction in amplifier gain. Since upconversion coefficient is not directly measurable, Hwang et al. and Lopez et al. respectively proposed a method to calculate it, which simulates the experimental fluorescence decay process by the decay of population N_2 at state $^4I_{13/2}$ after the withdraw of the pump [17, 18]:

$$N_2(t) = A_{21}^R \left[\left(\frac{A_{21}^R}{N_2(0)} + C \right) \exp\left(A_{21}^R t\right) - C \right]^{-1} \quad (1)$$

with $N_2(0)$ the steady-state population at $^4I_{13/2}$ after the long-time interaction of the pump:

$$N_2(0) = \frac{(R_{13}/A_{21}^R + 1)}{2C/A_{21}^R} \left[\sqrt{1 + \frac{4CNR_{13}/A_{21}^{R^2}}{(R_{13}/A_{21}^R + 1)^2}} \right] \quad (2)$$

where C is homogeneous upconversion coefficient. A_{21}^R is spontaneous emission rate between states $^4I_{13/2}$ and $^4I_{15/2}$. R_{13} is pumping rate of 980 nm laser. $N = 2.71 \times 10^{20}$ions/cm^3 is total Er^{3+} concentration.

The simulated results for different upconversion coefficient C 0.4×10^{-18}, 0.95×10^{-18}, and 2.0×10^{-18} cm^3/s are shown in Fig. 14, respectively. It can be seen that the simulated curve for $C = 0.95 \times 10^{-18}$ cm^3/s matches the experimental result best. Eventually, we found the

Table 1 Comparison of upconversion coefficients in different host materials

Host	N(ions/cm^3)	C($\times 10^{-18}$ cm^3/s)
Yb-Er-SBA-15	2.71×10^{20}	0.9–1.1
Phosphate [17]	2×10^{19}-4×10^{20}	0.8–1.1
Soda-lime silicate waveguide [17]	1×10^{20}	3.8
Er-implanted Al_2O_3 waveguide [17]	1.2×10^{20}	4
Alumino-silicate [17]	7×10^{19}-4×10^{20}	0.5–2

simulation curve matches well with the experiment in the range of 0.9–1.1 $\times$ 10^{-18} cm^3/s for C, which is similar to the upconversion coefficient in phosphate glass as shown in Table 1.

The upconversion effect, induced by the aggregation of Er^{3+} ions and causing the gain reduction, is more serious in the densely Er^{3+} doped case. To avoid this, it is important to separate Er^{3+} ions. In Yb-Er-SBA-15, two mechanisms correspond to the separation of Er^{3+} ions. They are (1) walls of mesopores and cages for those Er^{3+} ions located in different mesopores and cages; (2) Yb^{3+} ions for those Er^{3+} ions located in the same mesopore or cage. These two mechanisms explain why upconversion effect in Yb-Er-SBA-15 is relatively weak.

Analyses Judd–Ofelt Parameters

The Judd–Ofelt theory is usually used to evaluate the transition probability of rare-earth ions in various environments and to calculate the spectroscopic parameters [19]. It has been shown that for glass materials the Judd–Ofelt parameters are of dependence to the local structure in the vicinity of rare-earth ions and to the basicity of rare-earth sites. Such dependence is useful in estimating the emission properties of rare-earth-doped glass [20]. The Judd–Ofelt theory can also be used to study the mesoporous silica with a well-ordered pore arrangement and symmetry because it has similarity in material composition with fully disordered silica though different in structure.

The transitions between the energy states, that meet the selection rules $\Delta S = \Delta L = 0$, $\Delta J = 0, \pm 1$, may include the contribution from both electric-dipole transition S^{ed} and magnetic-dipole transition S^{md} which can be given by

$$S^{ed} = \sum_{t=2,4,6} \Omega_t \left| \langle \gamma J \| U^{(t)} \| \gamma' J' \rangle \right|^2 \tag{3}$$

$$S^{md} = \frac{1}{4m^2c^2} \left| \langle \gamma J \| L + 2S \| \gamma' J' \rangle \right|^2 \tag{4}$$

where while $J' = J - 1$, J and $J + 1$, matrix element $\langle \gamma J \| L + 2S \| \gamma' J' \rangle$ is given respectively by

$$\hbar \left\{ [(S + L + 1)^2 - J^2][J^2 - (L - S)^2]/(4J) \right\}^{1/2} \tag{5}$$

$$\hbar \{(2J + 1)/[4J(J + 1)]\}^{1/2} [S(S + 1) - L(L + 1) + 3J(J + 1)] \tag{6}$$

$$\hbar \left\{ [(S + L + 1)^2 - (J + 1)^2] [(J + 1)^2 - (L - S)^2]/[4(J + 1)] \right\}^{1/2} \tag{7}$$

It can be discerned that S^{md} is constant and independent to the ligand fields and S^{ed} is a function of glass structure and composition [21]. For the transitions, for instance $^4I_{13/2} \rightarrow {}^4I_{15/2}$, with $\Delta J = 1$ in total angular momentum, there exists the contribution from the magnetic-dipole transition [22]. It is often considered that a larger relative contribution from the magnetic-dipole transition results in a narrower 1.55 μm emission spectrum [21]. To obtain flat and broad emission spectra, it is effective to increase the relative contribution of the electric-dipole transition. The line strength of the electric-dipole components for $^4I_{13/2} \rightarrow {}^4I_{15/2}$ transition of Er^{3+} ions in Eq. 3 can be further expressed as [23]

$$S^{ed}\left({}^4I_{13/2} : {}^4I_{15/2}\right) = 0.0188\Omega_2 + 0.1176\Omega_4 + 1.4617\Omega_6 \tag{8}$$

In this equation, Ω_6 is dominant and a larger Ω_6 produces a larger S^{ed} value, consequently a broader emission bandwidth [24] and an increased radiative transition probability [25]. Theoretically, the intensity parameters Ω_{t} can be represented by [26]

$$\Omega_t = (2t + 1) \sum_{p,s} \left| A_{sp} \right|^2 \Xi^2(s, t)(2s + 1)^{-1} \tag{9}$$

where A_{sp} are the sets of odd-parity terms of the crystal field and $\Xi(s, t)$ are functions of radial overlap integrals $\langle 4f | r^s | nl \rangle$. It is proved that Ω_6 can be more greatly affected by the change of the integrals than Ω_2 and Ω_4, and accordingly is more sensitive to the change of electron density of the *4f* and *5d* orbitals, while Ω_2 is more sensitive to A_{sp} [25]. The integral $\langle 4f | r^s | 5d \rangle$ decreases with the increased *6s* electron density because of the shield or repulse of the *5d* orbital by the *6s* electrons. The *6s* electron density increases with increasing covalency of the Er–O bond or the local basicity of Er^{3+} site in host materials [27]. Consequently, $\langle 4f | r^s | nl \rangle$ and accordingly the values of Ω_t become small with an increase in the basicity [28]. In PMS functionalized SBA-15, no alkali-metals exist. The basicity is not strong and is affected by the existence of the residual acetate ions with a relatively high acidity and also the hydroxyl groups with a weak acidity. In Table 2, the Ω_{t} (t = 2, 4, 6) parameters of Er(PMS)$_{\mathrm{x}}$ complex in SBA-15 and Er^{3+} in other glass hosts are listed. It can be seen that Ω_6 in Er(PMS)$_{\mathrm{x}}$-SBA-15 is larger than those in germinate, silicate, aluminate, and phosphate glass but smaller than

Table 2 Comparison of $\Omega_t(t = 2, 4, 6)(\times 10^{-20}\text{cm}^2)$ of Er^{3+} in some host materials

Host material	Ω_2	Ω_4	Ω_6
Germanate glass [29]	5.81	0.85	0.28
Fluorophosphate glass [29]	2.91	1.63	1.26
Silicate glass [29]	4.23	1.04	0.61
Aluminate glass [29]	5.60	1.60	0.61
Fluoride glass [29]	2.91	1.27	1.11
Phosphate glass [30]	3.89	1.01	0.55
Tellurite glass [31]	5.05	1.45	1.22
Bismuth-based glass [32]	3.86	1.52	1.17
$Er(PMS)_x$-SBA-15	1.04	2.38	1.06

those in fluorophosphate, fluoride, tellurite, and bismuth-based glass. This indicates that the Er–O bond in $Er(PMS)_x$-SBA-15 is less covalent and less basic than those in germinate, silicate, aluminate, and phosphate glass but more covalent and more basic than those in fluorophosphate, fluoride, tellurite, and bismuth-based glass.

It has been reported that Ω_2 is closely related to the hypersensitive transitions $^2H_{11/2} \leftarrow {}^4I_{15/2}$ and $^4G_{11/2} \leftarrow {}^4I_{15/2}$ for Er^{3+} ions [26], namely, a stronger hypersensitive transition corresponds to a larger value of Ω_2. Jørgensen and Judd [33] also reported that the hypersensitivity of certain lines in the spectra of rare-earth ions arises from the inhomogeneity of the environment of rare-earth ions and the most striking effect is expected for highly polarized and asymmetric environment around rare-earth ions. In our case, SBA-15 contains many highly ordered and symmetric mesopores, although its silica walls are amorphous. No doubt, SBA-15 is with a higher content of orderliness in comparison with those fully disordered and asymmetric glass materials in Table 2. This contributes to relatively weaker hypersensitive transitions $^2H_{11/2} \leftarrow {}^4I_{15/2}$ and $^4G_{11/2} \leftarrow {}^4I_{15/2}$ for Er^{3+} ions in $Er(PMS)_x$-SBA-15, and furthermore results in a smaller value of Ω_2 in Table 2. Our experiments (see Fig. 7) also show that the hypersensitive transitions $^2H_{11/2} \leftarrow {}^4I_{15/2}$ and $^4G_{11/2} \leftarrow {}^4I_{15/2}$ in $Er(PMS)_x$-SBA-15 are less intense than those in Er-SBA-15. This indicates that the shrinkage of SBA-15 sieve framework introduced by PMS (see Fig. 2) somewhat destroys the mesostructure order of SBA-15 background.

In addition, similar results can be obtained for Yb-Er-SBA-15 for upconversion coefficient and Judd–Ofelt parameters.

Conclusions

$Er(PMS)_x$ functionalized mesoporous SBA-15 and Yb^{3+}/Er^{3+}-codoped SBA-15 have been fabricated and characterized. Both of these two complexes exhibit intense near-IR luminescence with large peak emission cross section $\sigma_{em} = 10.9 \times 10^{-21}\text{cm}^2$ and $\sigma_{em} = 11.17 \times 10^{-21}\text{cm}^2$, respectively. Compared with the peak emission cross section $\sigma_{em} = 7.9 \times 10^{-21}\text{cm}^2$ of Er^{3+} in conventional silica, the above results have 27.5 and 29.3% increase, respectively. This is attributed to the low-vibration environment created by PMS or efficient sensitization of Yb^{3+} to Er^{3+}. The effective separation of Er^{3+} ions, obtained from the walls and cages of mesopores, and the ligating with PMS or codoped Yb^{3+} ions, makes the upconversion effect relatively weak. Although $Er(PMS)_x$-SBA-15 does not have extremely attractive bandwidth for the amplifier application in optical communications, Yb-Er-SBA-15 has 88 nm broad "effective bandwidth". The high emission cross section and broad "effective bandwidth" makes them good candidates for the applications of high output lasers or broadband amplifiers.

Acknowledgments The authors thank Professor Chunhua Yan from School of Chemistry, Beijing University for helpful discussion. The authors also thank Liqiong An from Shanghai Institute of Ceramics, Chinese Academy of Sciences, Meiying Huang and Shunguang Li from Shanghai Institute of Optics and Fine Mechanics, Chinese Academy of Sciences, and Zhigao Hu from East China Normal University for some measurements. This research was financially supported by the Science and Technology Commission of Shanghai under grants 05JC14069 and 09XD1401500, National Fundamental Research Program of China (973 Program) under grant 2006CB921100, the NSFC of China (20925310), and Specialized Research Fund for the Doctoral Program of Higher Education (20070269023).

References

1. Q.G. Meng, P. Boutinaud, A.-C. Franville, H.J. Zhang, R. Mahiou, Preparation and characterization of luminescent cubic MCM-41 impregnated with an Eu^{3+} β-diketonate complex. Microporous Mesoporous Mater. **65**, 127–136 (2003)
2. M. Alvaro, V. Forne's, S. Garcı'a, H. Garcı'a, J.C. Scaiano, Intrazeolite photochemistry. 20. Characterization of highly luminescent europium complexes inside zeolites. J. Phy. Chem. **102**, 8744–8750 (1998)
3. D. Zhao, J. Feng, Q. Huo, N. Melosh, G.H. Fredrickson, B.F. Chmelka, G.D. Stucky, Triblock copolymer syntheses of mesoporous silica with periodic 50–300 angstrom pores. Science **279**, 548–552 (1998)
4. S. Gago, J.A. Fernandes, J.P. Painho, R.A.S. Ferreira, M. Pillinger, A.A. Valente, T.M. Santos, L.D. Carlos, P.J. Riberro-Claro, I.S. Goncalves, Highly luminescent Tris(â-diketonate)europium(III) complexes immobilized in a functionalized mesoporous silica. Chem. Mater. **17**, 5077–5084 (2005)
5. L. Sun, H. Zhang, C. Peng, J. Yu, Q. Meng, L. Fu, F. Liu, X. Guo, Covalent linking of near-infrared luminescent ternary lanthanide (Er3+, Nd3+, Yb3+) complexes on functionalized mesoporous MCM-41, SBA-15. J. Phys. Chem. **110**, 7249–7258 (2006)

6. L. Sun, H. Zhang, J. Yu, S. Yu, C. Peng, S. Dang, X. Guo, J. Feng, Near-infrared emission from novel Tris(8-hydroxyquinolinate)lanthanide(III) complexes-functionalized mesoporous SBA-15. Langmuir **24**, 5500–5507 (2008)
7. Y. Wada, T. Okubo, M. Ryo, T. Nakazawa, Y. Hasegawa, S. Yanagida, High efficiency near-IR emission of Nd(III) based on low-vibrational environment in cages of nanosized zeolites. J. Am. Chem. Soc. **122**, 8583–8584 (2000)
8. M. Ryo, Y. Wada, T. Okubo, Y. Hasegawa, S. Yanagida, Intrazeolite nanostructure of Nd(III) complex giving strong near-infrared luminescence. J. Phys. Chem. **107**, 11302–11306 (2003)
9. S. Comby, D. Imbert, A.-.S. Chauvin, J.-.C.G. Bunzli, Stable 8-hydroxyquinolinate-based podates as efficient sensitizers of lanthanide near-infrared luminescence. Inorg. Chem. **45**(2), 732–743 (2006)
10. G.C. Valley, Modeling cladding-pumped Er/Yb fiber amplifiers, modeling cladding-pumped er/yb fiber amplifiers. Opt. Fiber Technol. **7**, 21–44 (2001)
11. D.H. Everett, Pure Appl. Chem. **31**, 577 (1972)
12. J.R. Bartlett, R.P. Cooney, R.A. Kydd, Europium-exchanged synthetic faujasite zeolites: A luminescence spectroscopic study. J. Catal. **114**, 58–70 (1988)
13. M. Alvaro, V. Fornes, S. Gareia, H. Gareia, J.C. Seaiano, Intrazeolite Photochemistry 20. Characterization of highly luminescent europium complexes inside zeolites. J. Phys. Chem. B **102**, 8744–8750 (1998)
14. W.L. Barnes, R.I. Laming, E.J. Tarbox, P.R. Morkel, Absorption and emission cross section of Er^{3+} doped silica fibers. IEEE. J. Quantum. Electron **27**, 1004–1010 (1991)
15. W. Zhang, M. Yi, Preparation and properties of nanometric scale luminescent materials doped by rare earth. Chin. J. Lumin **21**, 314–319 (2000)
16. J.C. Wright, in *Radiationless Processes in Molecules and Condensed Phases*, vol. 4, ed. by F.K. Fong (Springer-Verlag, Berlin, 1976)
17. B. Hwang, S. Jiang, T. Luo et al., Cooperative upconversion and energy transfer of new high Er^{3+}- and Yb^{3+}-Er^{3+} doped phosphate glasses. J. Opt. Soc. Am. B **17**(5), 833–839 (2000)
18. V. Lopez, G. Paez, M. Strojnik, Characterization of upconversion coefficient in erbium-doped materials. Opt. Lett. **31**(11), 1660–1662 (2006)
19. K. Soga, H. Inoue, A. Makishima, Calculation, simulation of spectroscopic properties for rare earth ions in chloro-fluorozirconate glasses. J. Non-Cryst. Solids **274**, 69–74 (2000)
20. S. Tanable, T. Ohyagi, N. Soga, T. Hanada, Compositional dependence of Judd-Ofelt parameters of Er^{3+} ions in alkali-metal borate glasses. Phys. Rev. B **46**, 3305–3310 (1992)
21. S. Tanable, Optical transitions of rare earth ions for amplifiers: How the local structure works in glass. J. Non-Cryst. Solids **259**, 1–9 (1999)
22. W.T. Carnall, P.R. Fields, K. Rajnak, Electronic energy levels in the trivalent lanthanide aquo ions. I. Pr^{3+}, Nd^{3+}, Pm^{3+}, Sm^{3+}, Dy^{3+}, Ho^{3+}, Er^{3+}, Tm^{3+}. J. Chem. Phys. **49**, 4424–4442 (1968)
23. M.J. Weber, Probabilities for radiative, nonradiative decay of Er^{3+} in LaF3. Phys. Rev. **157**, 262–272 (1967)
24. J. Yang, S. Dai, N. Dai, S. Xu, L. Wen, L. Hu, Z. Jiang, Effect of Bi2O3 on the spectroscopic properties of erbium-doped bismuth silicate glasses. J. Opt. Soc. Am. B **20**, 810–815 (2003)
25. S. Tanabe, T. Hanada, T. Ohyagi, N. Soga, Correlation between ^{151}Eu Mossbauer isomer shift, Judd-Ofelt Ω_6 parameters of Nd^{3+} ions in phosphate, silicate laser glasses. Phy. Rev. B **48**, 10591–10594 (1993)
26. R.D. Peacock, in *Structure and Bonding*, vol. 22, ed. by J.D. Dunitz, et al. (Spring-Verlag, Berlin, 1975), p. 83
27. S. Tanabe, K. Hirao, N. Soga, Mössbauer spectroscopy of ^{151}Eu in oxide crystals and glasses. J. Non-Cryst. Solids **113**, 178–184 (1989)
28. S. Tanabe, T. Ohyagi, N. Soga, T. Hanada, Compositional dependence of Judd-Ofelt parameters of Er^{3+} ions in alkali-metal borate glasses. Phy. Rev. **46**, 3305–3310 (1992)
29. X. Zou, T. Izumitani, Spectroscopic properties, mechanisms of excited state absorption, energy transfer upconversion for Er^{3+} -doped glasses. J. Non-Cryst. Solids **162**, 68–80 (1993)
30. G.C. Righini, S. Pelli, M. Fossi, M. Brenci, A.A. Lipovskii, E.V. Kolobkova, A. Speghini, M. Bettinelli, Characterization of Er-doped sodium-niobium phosphate glasses, *Rare-Earth-Doped Materials and Devices V*, Jiang S., ed., 2001, *Proceedings of. SPIE* vol **4282**, 210–215
31. X. Feng, S. Tanabe, T. Hanada, Spectroscopic properties, thermal stability of Er^{3+} -doped germanotellurite glasses for broadband fiber amplifiers. J. Am. Ceram. Soc. **84**, 165–171 (2001)
32. S. Tanabe, N. Sugimoto, S. Ito, T. Hanada, Broadband 1.5 μm emission of Er^{3+} ions in bismuth-based oxide glasses for a potential WDM amplifier. J. Lumin. **87 & 89**, 670–672 (2000)
33. C.K. Jørgensen, B.R. Judd, Hypersensitive pseudoquadrupole transitions in lanthanides. Mol. Phys. **8**, 281–290 (1964)